Supplementary information

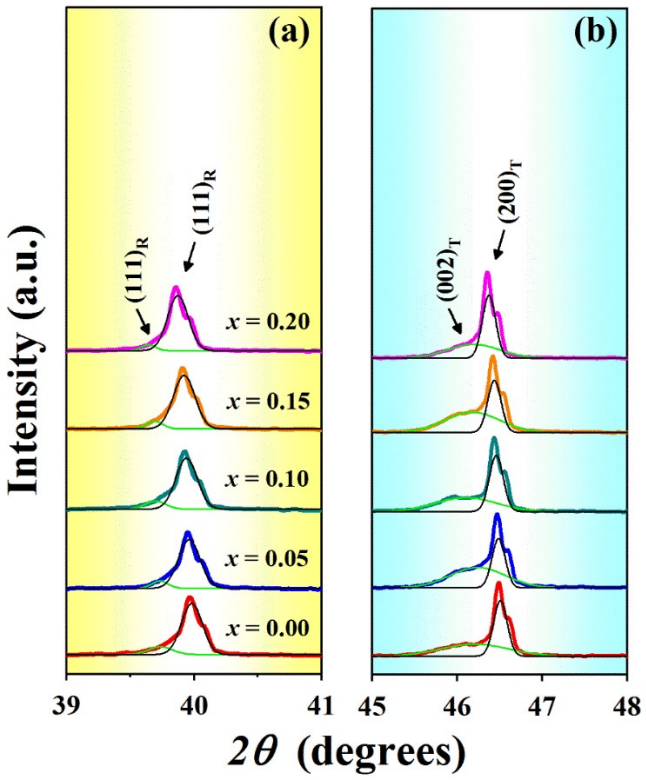

Fig. S1. XRD patterns of the ceramics at (a) 2θ = 39 – 41° and (b) 2θ = 45 – 48°.

X-ray diffraction (XRD) patterns of the ceramics, recorded over the range 2θ = 20 – 70°, are presented in the main text. The observed diffraction peaks correspond well to the structure reported in JCPDS file No. 36-0340. A specific JCPDS file for SBT is not available because it is a solid solution rather than a single-phase compound; however, its crystal structure adopts a perovskite-type arrangement similar to its parent compound $SrTiO_3$ (JCPDS file No. 35-0734). Similarly, no JCPDS file exists for STZ. XRD patterns of the ceramics at (a) 2θ = 39 – 41° and (b) 2θ = 45 – 48° are shown in Fig. S1. All samples exhibited peak splitting near 2θ = 39 – 41° ($(111)_R/(1\bar{1}1)_R$) and 45 – 48° ($(200)_T/(002)_T$), as shown in Fig. S1(a) and (b), respectively. This indicates the coexistence of rhombohedral (R) and tetragonal (T) phases.

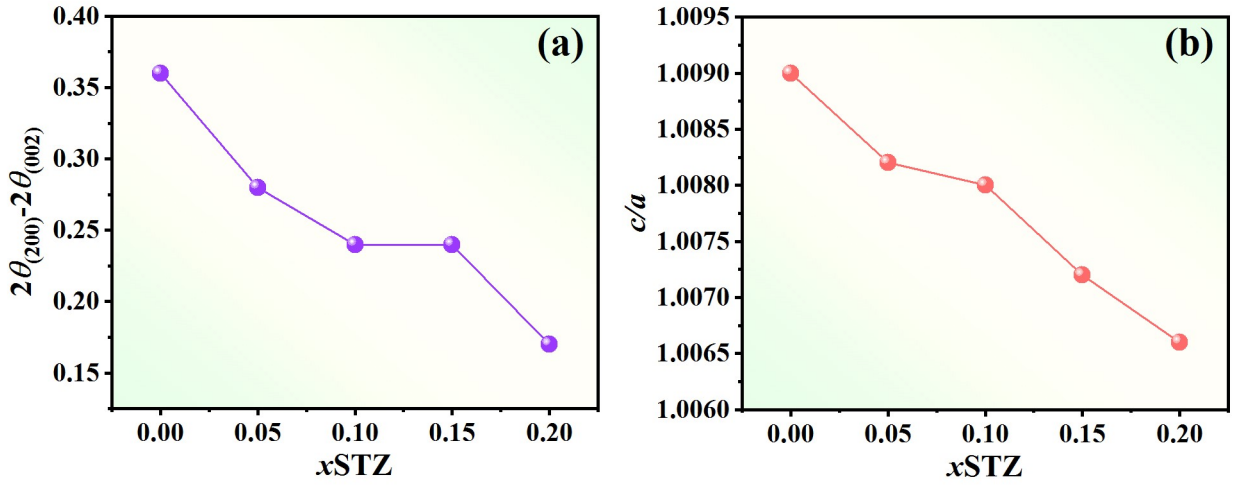

Fig. S2. (a) $\Delta 2\theta_{200} = 2\theta_{(200)} - 2\theta_{(002)}$, and (b) tetragonality (c/a) versus of x

The values of $\Delta 2\theta_{200} = 2\theta_{(200)} - 2\theta_{(002)}$ and tetragonality (c/a) as a function of x are presented in Fig. S2. Both parameters decrease with increasing x, indicating a progressive shift toward a more cubic structure and reduced tetragonality.

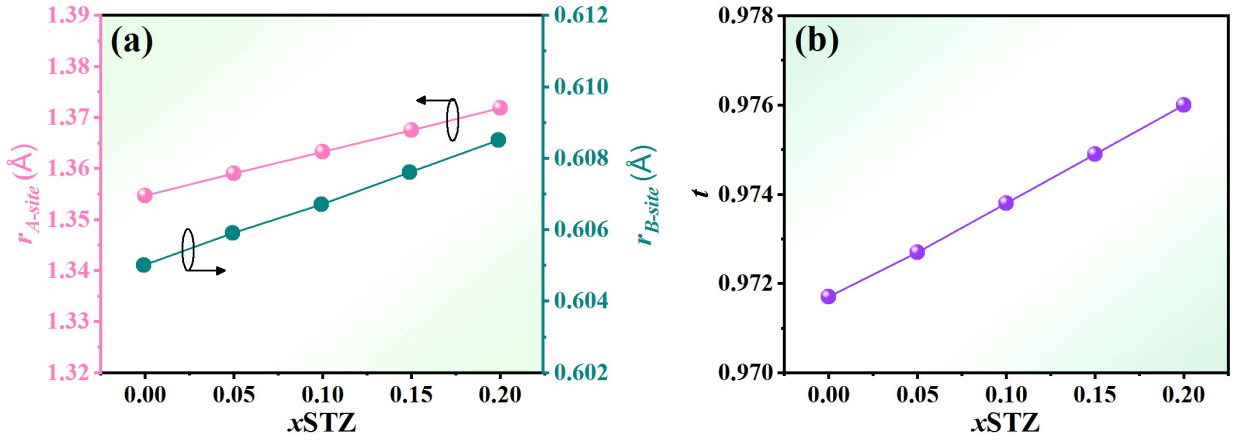

Fig. S3. (a) $r_{A\text{-}site}$ and $r_{B\text{-}site}$ and (b) t factors as a function of x

In this work, the average ionic radius of the A-and B-site ions (r_{A-site} and r_{B-site}) of the ceramics was calculated from the equation:

$$r_{A-site} = x\left[r_{Sr^{2+}}\right] + (1-x)[0.35r_{Bi^{3+}} + 0.35r_{Na^{+}} + 0.21r_{Sr^{2+}} + 0.6r_{Bi^{3+}}] \quad \text{(S1)}$$

and

$$r_{B-site} = x\left[0.85r_{Ti^{4+}} + 0.15r_{Zr^{4+}}\right] + (1-x)[0.7r_{Ti^{4+}} + 0.3r_{Ti^{4+}}] \quad \text{(S2)}$$

,where $r_{Sr^{2+}}$, $r_{Bi^{3+}}$, $r_{Na^{+}}$, $r_{Ti^{4+}}$, and $r_{Zr^{4+}}$ are ionic radii of Sr, Bi, Ti, and Zr, respectively. Fig. S3 presents $r_{A\text{-}site}$ and $r_{B\text{-}site}$ values as a function of x. The $r_{A\text{-}site}$ and $r_{B\text{-}site}$ values increased with increasing x. To determine the lattice distortion, a simple description of the geometric packing within the perovskite structure can be characterized by the tolerance factor (t), which is defined by the following equation [S1,S2]:

$$t = \frac{(r_{A-site} + r_O)}{\sqrt{2}(r_{B-site} + r_O)} \quad \text{(S3)}$$

, where r_A, r_B and r_O are the ionic radii of A-site cations, B-site cations, and the oxygen anion, respectively. In this work, Shannon ionic radii were used: Bi^{3+} (C.N. = 12) = 1.38 Å, Na^{+} (C.N. = 12) = 1.39 Å, Sr^{2+} (C.N. = 12) = 1.44 Å, Ti^{4+} (C.N. = 6) = 0.605 Å, Zr^{4+} (C.N. = 6) = 0.72 Å, and O^{2-} (C.N. = 6) = 1.40 Å. When t = 1, a perfect cubic cell is formed, and when t deviates from 1, the perovskite cell gets deformed [S2]. The tolerance factor (t) was calculated for each composition and found to increase progressively with increasing x, ranging from 0.9717 to 0.9782. This range lies well within the typical stability window for perovskite structures (t = 0.880 – 1.090) [S3],

suggesting that all compositions maintain a structurally stable perovskite phase. This trend is illustrated in Fig. S3(b). It should be noted that the c/a ratio and the tolerance factor exhibit opposite trends. The tolerance factor increases with x because Sr and Zr enlarge the effective A- and B-site ionic radii, shifting the structure toward a more cubic configuration. In contrast, tetragonality decreases since the incorporation of Sr^{2+} and Zr^{4+} suppresses the off-centering of Bi and Ti, thereby reducing lattice distortion symmetry. Meanwhile, tetragonality decreases since Sr^{2+} and Zr^{4+} reduce Bi- and Ti off-centering.

Table S1. Phase formation refinement results of the studied ceramics

x	**0.00**		**0.05**		**0.10**		**0.15**		**0.20**	
Space group	*R*3*c*	*P*4*bm*	*R*3*c*	*P*4*bm*	*R*3*c*	*P*4*bm*	*R*3*c*	*P*4*bm*	*R*3*c*	*P*4*bm*
Phase frac. (%)	41	59	58	42	64	36	66	34	78	22
x^2	1.91		1.41		1.99		1.37		1.98	
R_w **(%)**	11.62		9.80		13.18		9.60		11.68	

Table S1 provides the Rietveld refinement data obtained using the GSAS-II software. The corresponding results, illustrated in Fig. 2(b-f), confirm the phase evolution across the samples. All compositions exhibited a coexistence of rhombohedral (*R3c*) and tetragonal (*P*4*bm*) phases. As the STZ content increased, the fraction of the rhombohedral *R3c* phase gradually rose, while the tetragonal *P*4*bm* phase diminished. This compositional shift is consistent with the observed decrease in the *c/a* ratio.

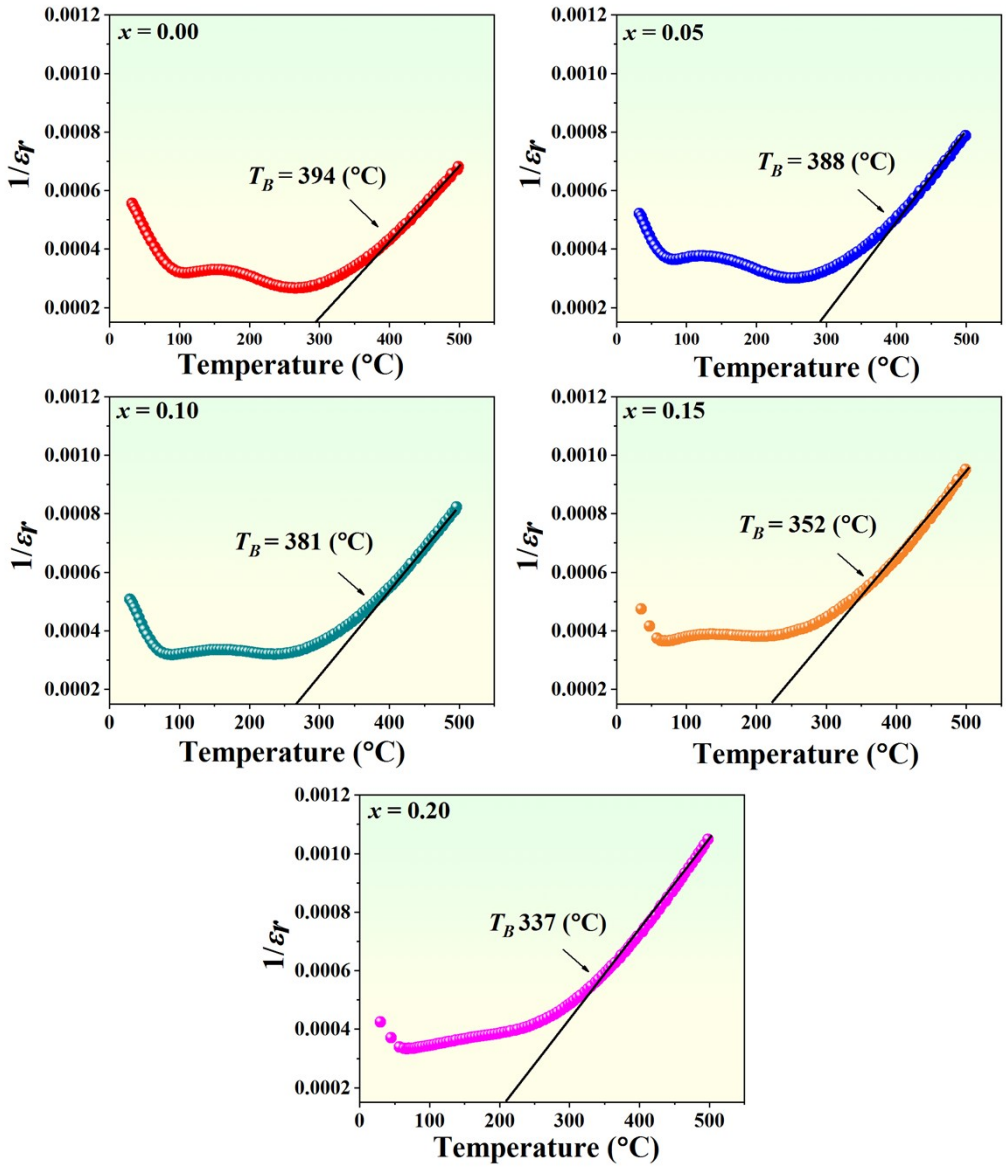

Fig. S4. Plots of $1/\varepsilon_r$ versus temperature of the samples.

The Burns temperature (T_B) denotes the point at which the dielectric constant begins to deviate from the Curie-Weiss law. In this work, T_B was determined from the $1/\varepsilon_r$ versus T plot, as shown in Fig. S4. The T_B values for BNT-SBT-xSTZ ceramics were observed to decrease with

increasing STZ content, specifically: 394 °C, 388 °C, 381 °C, 352 °C, 337 °C, and 326 °C for x = 0.00, 0.05, 0.10, 0.15, and 0.20, respectively.

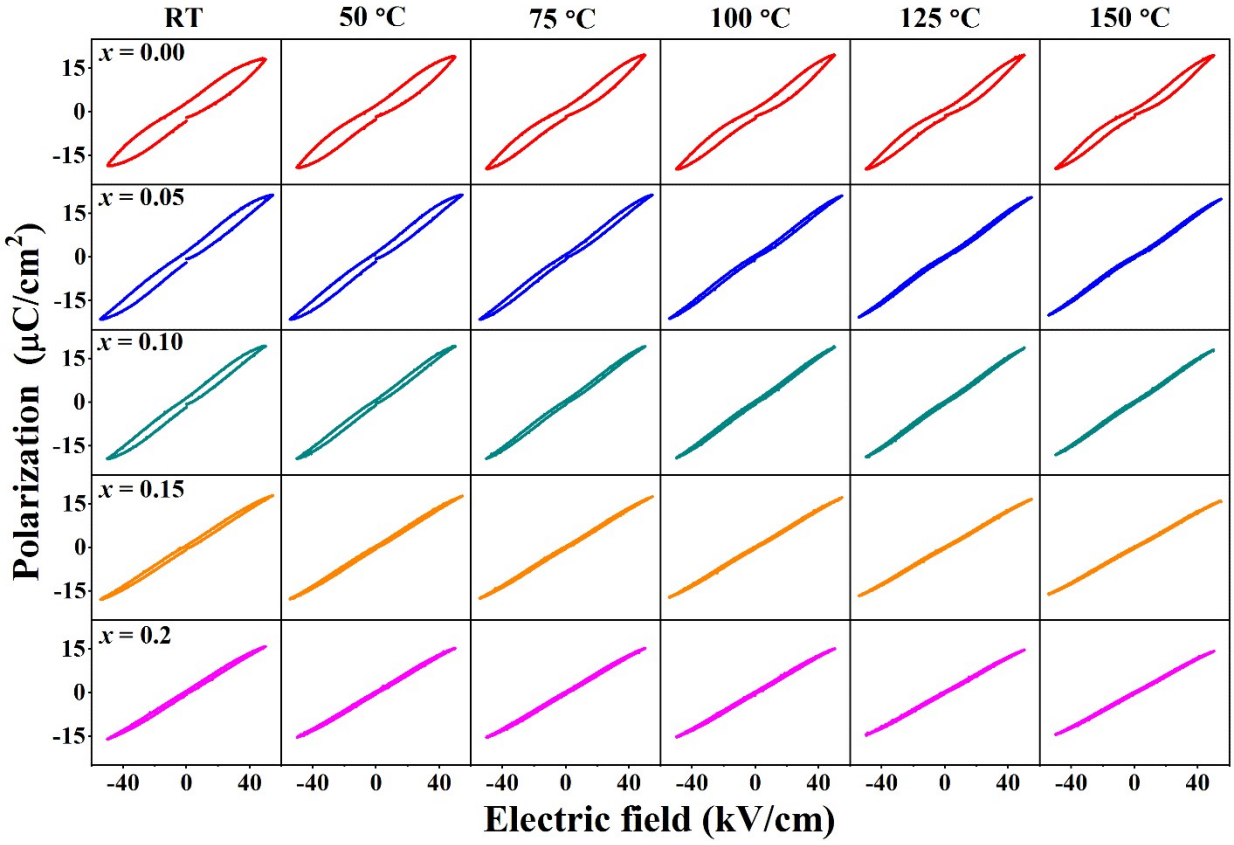

Fig. S5. Plots of polarization versus electric filed of the samples at various temperatures

Effects of temperature on the ferroelectric properties are presented in Fig. S5. Samples with compositions ranging from x = 0.00 to x = 0.15 exhibited slim and pinched P-E hysteresis loops, which are characteristic of ergodic relaxor ferroelectric behavior. The temperature-dependent P-E loops were measured from RT to 150°C under 50 kV/cm. It can be seen that both P_{max} and P_r slightly increase with increasing temperature (Fig. 9). Furthermore, the x = 0.20 samples exhibited a very slim and barely visible pinched loop, indicating a further suppression of long-range ferroelectric order and a stronger tendency toward a relaxor state.

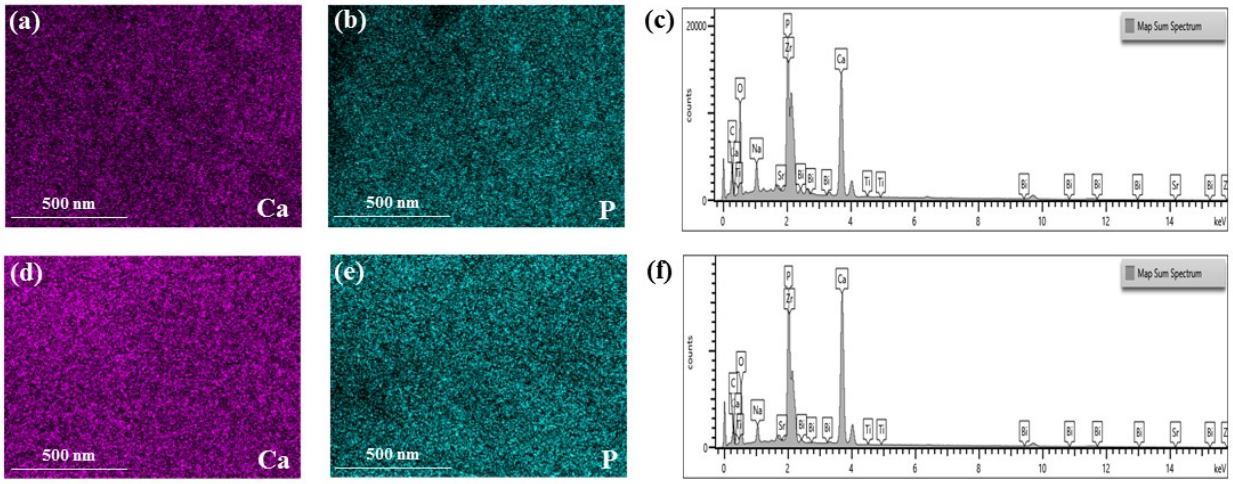

Fig. S6. EDS elemental mapping corresponding to Fig. 12(c) and (f), showing the apatite layer formed on the samples after immersion in SBF for 30 days: (a-c) uncoated sample and (d-f) β-TCP–coated sample, respectively.

The EDS analysis results of the apatite layer formed after immersion in SBF for 30 days are presented in Fig. S6, consistent with the surface morphology shown in Fig. 12(c and f). The EDS data confirmed the formation of an apatite layer, as indicated by the presence of calcium (Ca) and phosphorus (P), a key component of apatite, despite the fact that the original composition of the studied samples (0.85[BNT−SBT]-0.15STZ) does not contain Ca or P. Furthermore, the Ca/P ratio increased from 1.76 in uncoated samples to 2.05 in β-TCP-coated samples. Based on these EDS results, it can be concluded that bone-like apatite layers developed on the sample surfaces after immersion in SBF.

Table S2. Peak positions and full width at half maximum of Raman spectra of (1-*x*)[BNT-SBT]-*x*STZ ceramics.

Sample	The mode of Raman	A-site vibration	Ti-O Band		TiO_6 Octahedra		A1+E	
		P1	P2	P3	P4	P5	P6	P7
	Intensity (a.u.)	17071	17840	12667	10328	8570	1348	3005
***x* = 0.00**	Peak position (cm^{-1})	104	246	315	527	604	754	824
	FWHM (cm^{-1})	212	139	89	101	62	62	135
	Intensity (a.u.)	18645	17823	11642	10493	7602	1749	2521
***x* = 0.05**	Peak position cm^{-1})	103	250	314	527	603	755	830
	FWHM (cm^{-1})	217	139	89	112	65	82	111
	Intensity (a.u.)	17327	18426	13118	10493	8800	1639	2848
***x* = 0.10**	Peak position (cm^{-1})	106	250	314	526	603	755	830
	FWHM (cm^{-1})	204	134	94	99	69	76	112
	Intensity (a.u.)	19456	18694	12632	11048	8146	1808	2679
***x* = 0.15**	Peak position (cm^{-1})	106	251	312	526	601	755	829
	FWHM (cm^{-1})	203	134	95	112	72	74	112
	Intensity (a.u.)	21025	19274	12653	11305	7623	1818	2582
***x* = 0.20**	Peak position (cm^{-1})	105	252	311	525	599	756	831
	FWHM (cm^{-1})	202	131	98	114	74	78	108

The Raman spectra were deconvoluted using Lorentzian functions and the resulting modes were labeled P1 – P7. Table S2 summarizes the corresponding peak positions and full widths at half maximum (FWHM). The mode at ≤ 200 cm^{-1} (P1) is assigned to A-site cation vibrations of the perovskite lattice (Bi, Na and Sr). The modes in the 200 – 400 cm^{-1} region (P2 and P3) arise from Ti-O/(Ti,Zr)-O vibrations. As seen in Fig. 3, the P2 peak position shows almost no dependence on *x*, remaining in the range 246 – 252 cm^{-1} for all compositions, whereas the relative intensity of P3 gradually decreases with increasing STZ content. This reduction in P3 intensity is consistent with a decrease in the tetragonal *P*4*bm* fraction, in agreement with the XRD results [S4]. The FWHM of P2 exhibited a slight narrowing, whereas the P3 band showed an overall broadening as *x* increased (Table S2), indicating that the tetragonal-like local TiO_3 octahedral environments became increasingly disordered, even as their fraction decreased within the phase-coexistence region. In the 430 – 700 cm^{-1} range (P4 and P5), which corresponded to TiO_6 stretching vibrations in rhombohedral-like and tetragonal-like local structures, respectively, P5 displayed a clear increase in FWHM with increasing STZ content, whereas P4 showed only modest, non-monotonic changes. The progressive broadening of the P3 and P5 modes therefore reflects a high level of local structural disorder that strongly affects the dynamics of the TiO_3/$(Ti,Zr)O_3$ octahedra. The high-frequency modes above 700 cm^{-1} (P6 and P7) are attributed to overlapping A1(LO) and E(LO) bands [S5].

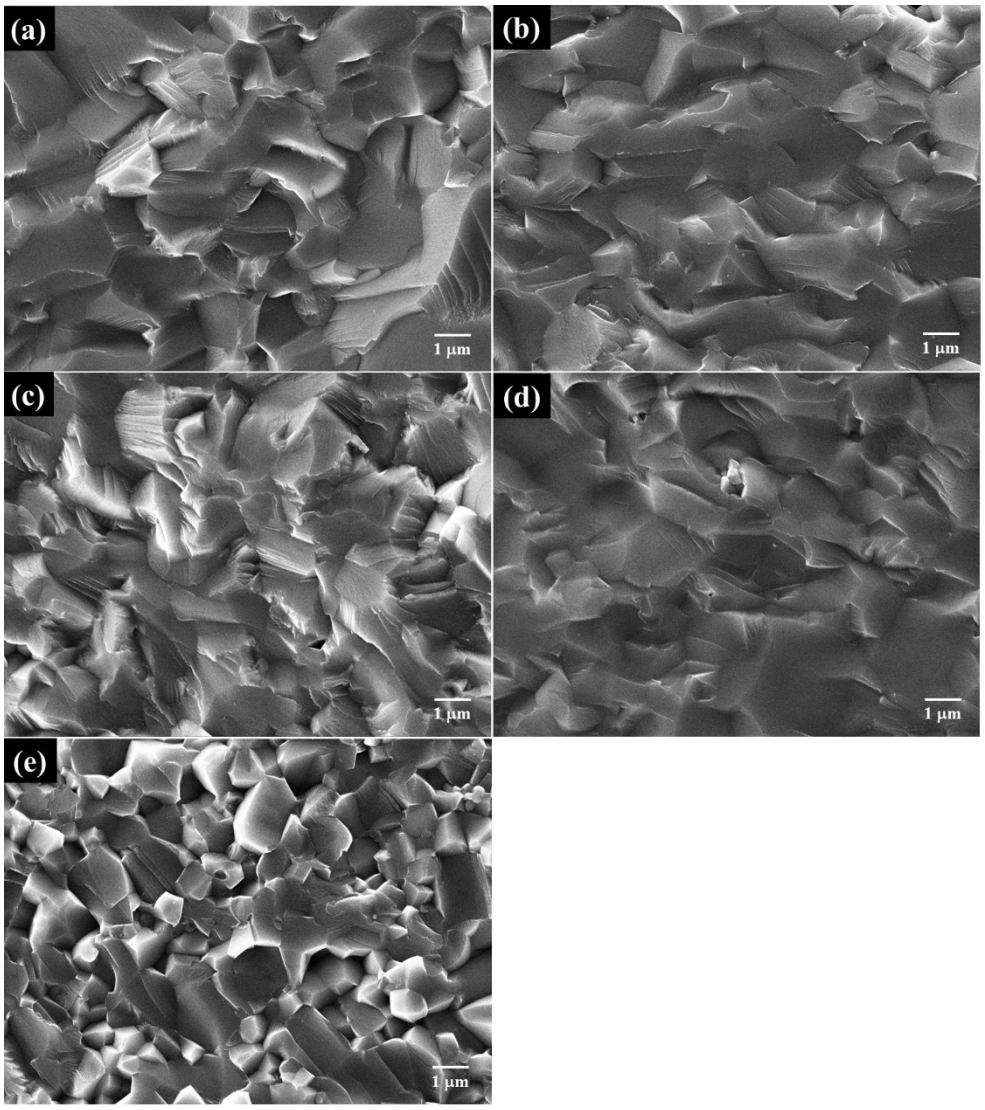

Fig. S7. SEM images of the cross-sections of the as-prepared (1-*x*)[BNT-SBT]-*x*STZ ceramics: (a) $x = 0.00$, (b) $x = 0.05$, (c) $x = 0.10$, (d) $x = 0.15$ and (e) $x = 0.20$

Fig. S7 shows that increasing the STZ content progressively refines the cross-sectional microstructure of the studied ceramics. The undoped sample exhibits course, irregular grains, whereas higher-*x* compositions ($x \geq 0.10$) develop smaller, more uniform, and more densely packed grains. This indicates that STZ addition effectively suppresses abnormal grain growth and promotes a fine, homogeneous microstructure.

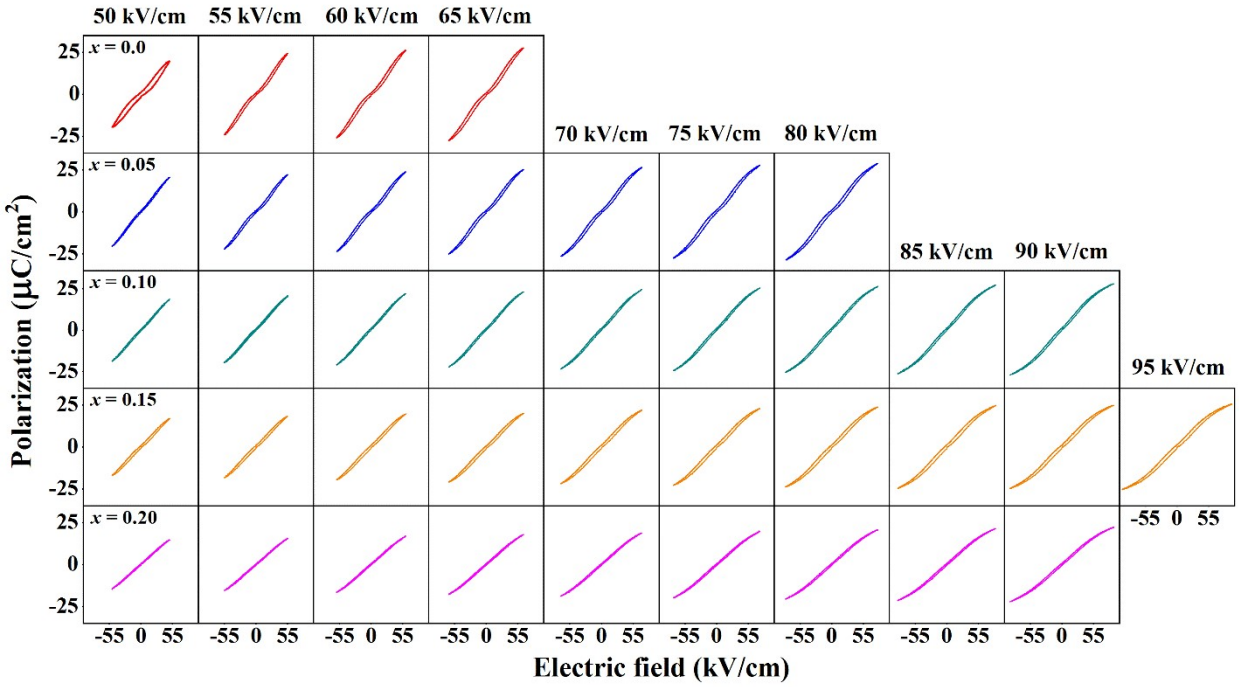

Fig. S8. Polarization-electric field (*P*-*E*) loops of the samples measured at 125 °C under different applied electric fields.

Fig. S8 illustrates how the *P*-*E* loops of the samples ($x = 0.00 – 0.20$) evolve with increasing electric field at 125 °C. As the field rises from 50 to 95 kV/cm, all compositions exhibit higher polarization, reflecting a stronger field-induced polarization response. Moreover, increasing the STZ content (higher x) results in progressively slimmer and more linear loops, indicating an enhanced ergodic relaxor character relative to the lower x compositions.

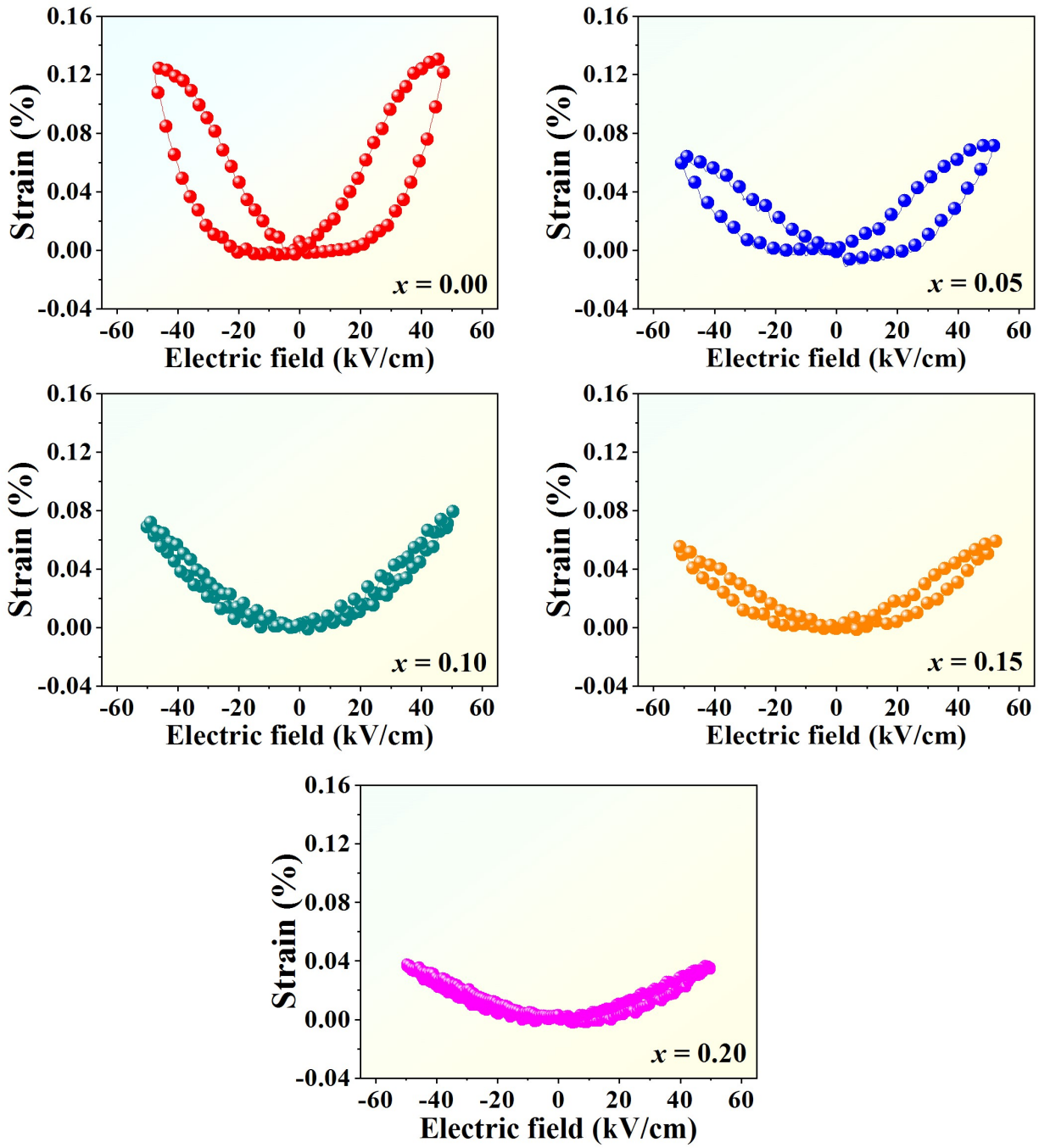

138

139 **Fig. S9.** Bipolar strain-electric field (*S*-*E*) loops of (1-*x*)[BNT-SBT]-*x*STZ ceramics, measured at

140 RT under an electric field of 50 kV/cm and a frequency of 1 Hz.

141 Fig. S9 presents the *S*-*E* loops of the (1–*x*)[BNT-SBT]-*x*STZ ceramics measured under an

142 electric field of 50 kV/cm at 1 Hz for compositions x = 0.00, 0.05, 0.10, 0.15, and 0.20. As

x increases, the maximum strain decreases, and the loops become progressively slimmer, indicating reduced ferroelectric ordering and enhanced relaxor behavior. For $x \geq 0.15$, the loops approach a nearly linear shape, consistent with a dominant ergodic relaxor phase and minimal remanent strain.

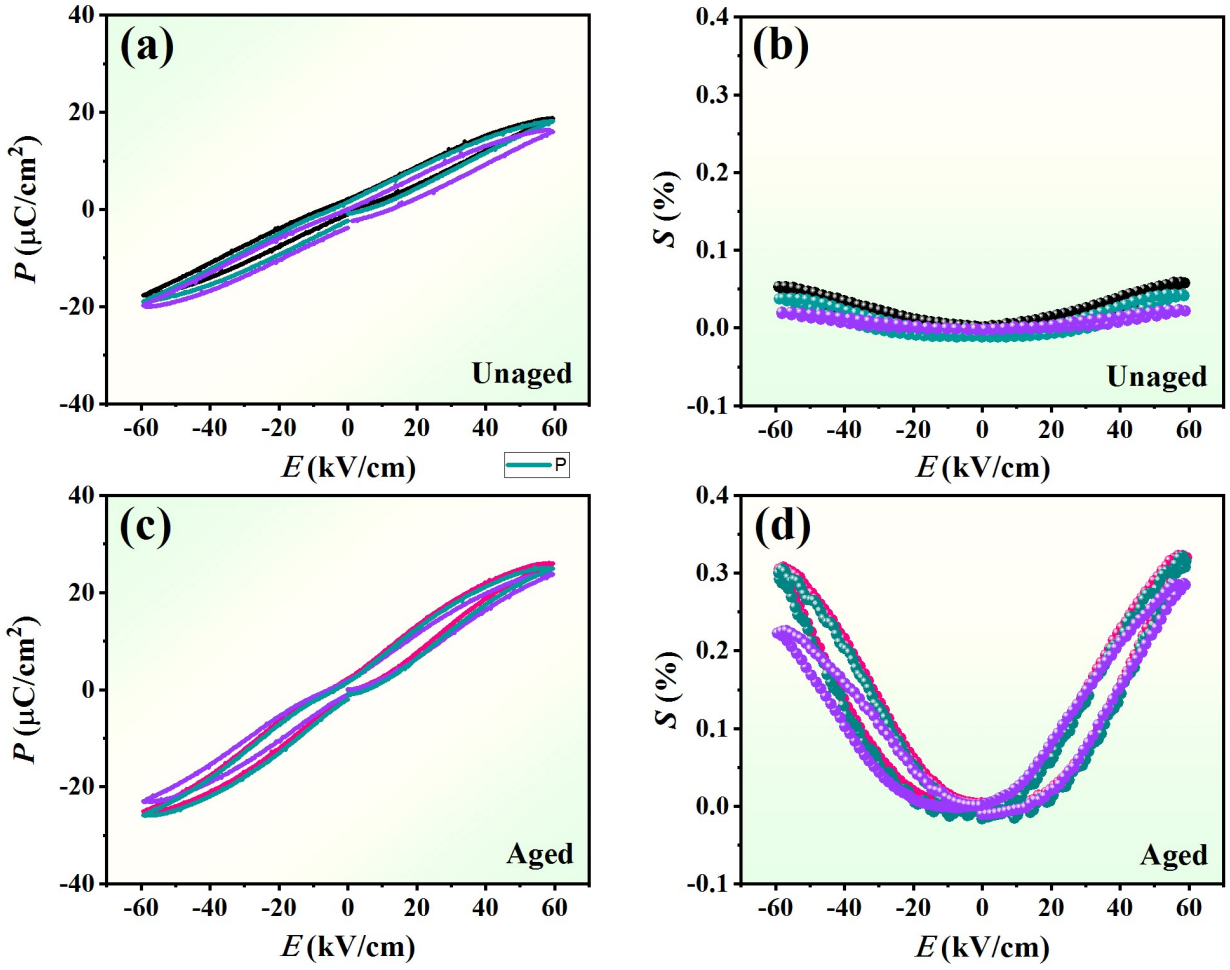

Fig. S10. (a-b) *P-E* hysteresis loops and (c-d) *S-E* loops for aged samples (x = 0.15), measured under an electric field of 60 kV/cm at 1 Hz from three repeated specimens (n = 3).

To ensure statistically reliable strain measurements, *P-E* and *S-E* loops were recorded three times. Fig. S10(a-b) shows the *P-E* hysteresis loops and bipolar *S-E* loops for unaged samples (x = 0.15), measured at RT under an electric field of 60 kV/cm at 1 Hz from three

repeated specimens (n = 3). Before annealing, the strain values were 0.03%, 0.05%, and 0.06%, with an average of 0.05% (Fig. S10(b)). After annealing, the strain values increased to 0.29%, 0.32%, and 0.33%, resulting in an average of 0.31% (Fig. S10(d)).

Table S3. Comparison of cell viability assay at 24 h.

Sample	**Cell viability (%)**	**Concentration (µg/ml)**	**Results**	**Ref.**
BNT-SBT-0.15STZ	>95	0.1 – 1000	Non-toxic	*This work*
10Co/HA/T coating	67	-	Non-toxic	84
HAp/AlN nanocomposites	>85	1000	Non-toxic	85
BG 1%FeS_2 and 3%FeS_2	>90	1000	Non-toxic	86
Glass-ceramics (50SiO_2-(45-X)CaO-($XTiO_2$)-5P_2O_5, X = 5, 7.5 and 10 wt %)	>90	12 – 50	Non-toxic	87
ZnO and DEP + ZnO NPs	-	15 – 25	Cytotoxicity	88

Table S3 provides a comparative summary of reported 24-h cell-viability results for different materials. The table lists the sample type, measured viability percentage, testing concentration range, and overall cytotoxicity outcome. The BNT-SBT-0.15STZ composition developed in this work shows >95% cell viability across a wide concentration range (0.1 – 1000 µg/mL), indicating a non-toxic response comparable to or better than previously reported materials such as Co/HA/Ti coatings, HAp/AlN nanocomposites, FeS_2-modified bioglasses, and SiO_3CaO-TiO_3 glass-ceramics. In contrast, ZnO and DEP+/ZnO nanoparticles exhibit cytotoxic behavior

even at relatively low concentrations. This comparison highlights the favorable biological performance and safety of the tested ceramics.

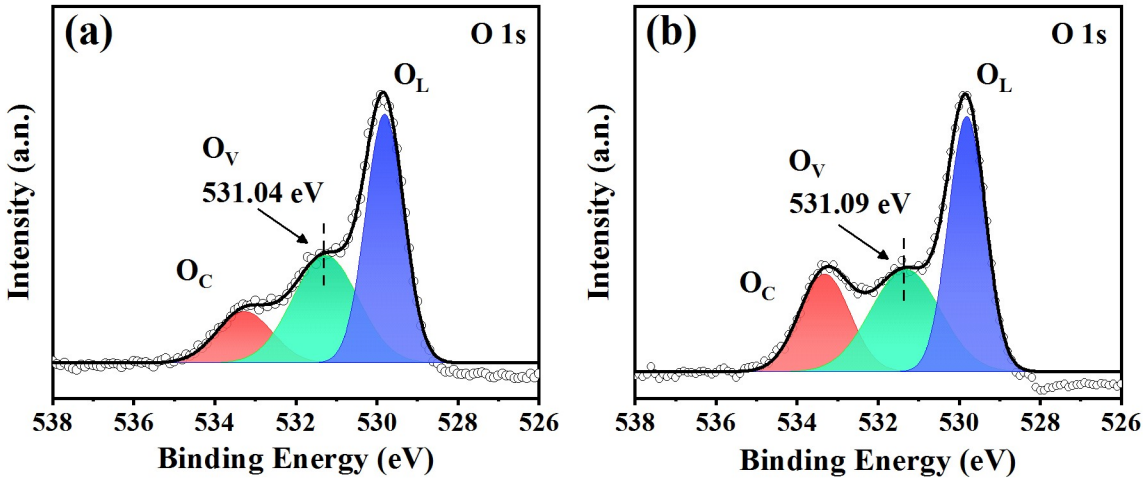

Fig. S11. High resolution XPS spectra of O 1s core levels of (a) unaged and (b) aged of BNT-SBT-0.15STZ ceramics.

Figure S11 shows the high-resolution XPS O 1s spectra of the studied ceramics before and after thermal aging at 120 °C. The O 1s peak can be separated into three components: lattice oxygen (O_L), adsorption oxygen (O_C), and the oxygen vacancy component (O_V) located near 531 eV. In the unaged sample, the presence of the O_V peak at 531.04 eV indicates that oxygen vacancies were already introduced during sintering. After thermal aging, the O_V peak position (531.09 eV) and its relative intensity remain almost unchanged. This indicates that aging at 120 °C, performed without any electrical treatment, is not sufficient to create new oxygen vacancies. Instead, the results suggest that the existing vacancies undergo only slight redistribution or stabilization during low-temperature aging. These XPS findings confirm that the changes in electrical behavior after aging originate from vacancy reorganization rather than an increase in vacancy concentration.

References

[S1] A. S. Bhalla, R. Guo, R. Roy, *Mater. Res. Innov*., 2000, **4**, 3–26.

[S2] Z. Li, M. Yang, J. S. Park, S. H. Wei, J. J. Berry, K. Zhu, *Chem. Mater*., 2016, **28**, 284−292.

[S3] K. S. Rao, K. C. V. Rajulu, B. Tilak, A. Swathi, *Nat. Sci*., 2010, **2**, 357–367.

[S4] Y. Mendez-González, A. Peláiz-Barranco, A.L. Curcio, A.D. Rodrigues, J.D.S. Guerra, *J. Raman Spectrosc*., 2019, 1–7.

[S5] X. Jia, J. Zhang, L. Wang, J. Wang, H. Du, Y. Yao, L. Ren, F. Wen, P. Zheng, *J Am Ceram. Soc*., 2019, **102**, 5203–5212.